RL-TR-95-74
In-House Report
April 1995
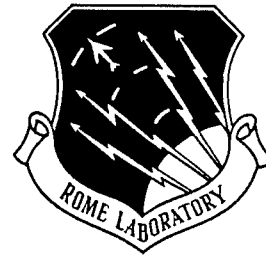
FREE SPACE DIGITAL OPTICAL PROCESSOR
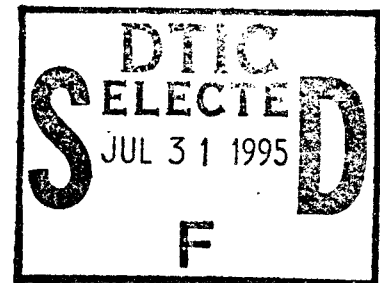
DTIC
SELECTED
JUL 3 1 1995
F

James M. Battiato, Rebecca J. Bussjager, Paul R. Cook
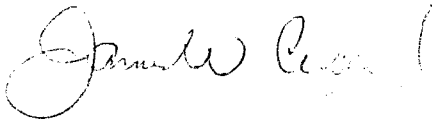
DTIC QUALITY INSPECTED 5

Rome Laboratory
Air Force Materiel Command
Griffiss Air Force Base, New York

19950728 034

This report has been reviewed by the Rome Laboratory Public Affairs Office (PA) and is releasable to the National Technical Information Service (NTIS). At NTIS it will be releasable to the general public, including foreign nations.
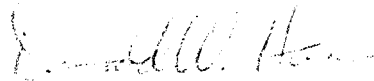
RL-TR-95-74 has been reviewed and is approved for publication.

APPROVED:

JAMES W. CUSACK, Chief
Photonics Division
Surveillance & Photonics Directorate

FOR THE COMMANDER:

DONALD W. HANSON
Director of Surveillance & Photonics

If your address has changed or if you wish to be removed from the Rome Laboratory mailing list, or if the addressee is no longer employed by your organization, please notify RL (OCPA) Griffiss AFB NY 13441. This will assist us in maintaining a current mailing list.

Do not return copies of this report unless contractual obligations or notices on a specific document require that it be returned.

REPORT DOCUMENTATION PAGE

Form Approved
OMB No. 0704-0188

1. AGENCY USE ONLY (Leave Blank)	2. REPORT DATE April 1995	3. REPORT TYPE AND DATES COVERED In-House Oct 91 – Sep 93

4. TITLE AND SUBTITLE FREE SPACE DIGITAL OPTICAL PROCESSOR	5. FUNDING NUMBERS PE - 62702F PR - 4600 TA - P3 WU - 11
6. AUTHOR(S) James M. Battiato, Rebecca J. Bussjager, Paul R. Cook	

7. PERFORMING ORGANIZATION NAME(S) AND ADDRESS(ES) Rome Laboratory (OCPA) 25 Electronic Pky Griffiss AFB NY 13441-4515	8. PERFORMING ORGANIZATION REPORT NUMBER RL-TR-95-74

9. SPONSORING/MONITORING AGENCY NAME(S) AND ADDRESS(ES) Rome Laboratory (OCPA) 25 Electronic Pky Griffiss AFB NY 13441-4515	10. SPONSORING/MONITORING AGENCY REPORT NUMBER

11. SUPPLEMENTARY NOTES

Rome Laboratory Project Engineer: James M. Battiato/OCPA (315) 330-7671

12a. DISTRIBUTION/AVAILABILITY STATEMENT Approved for public release; distribution unlimited.	12b. DISTRIBUTION CODE

13. ABSTRACT (Maximum 200 words)

The evaluation of the components used to construct a free space digital optical processor is presented. This processor is based on a gate-level optical inter-connect utilizing symmetric self-electro-optic effect devices (S-SEEDs) and vertical cavity surface emitting lasers (VCSELs). The evaluation of both the S-SEED devices and the electronics necessary to drive the microlaser array is performed. The design and construction of a diffractive optic interconnect is also presented.

14. SUBJECT TERMS Optical Computing, VCSELs, Photonics, Electro-optics, SEEDs, Free-space Interconnects	15. NUMBER OF PAGES 48
	16. PRICE CODE

17. SECURITY CLASSIFICATION OF REPORT UNCLASSIFIED	18. SECURITY CLASSIFICATION OF THIS PAGE UNCLASSIFIED	19. SECURITY CLASSIFICATION OF ABSTRACT UNCLASSIFIED	20. LIMITATION OF ABSTRACT U/L

1.0 INTRODUCTION

The increasing need for high speed processing systems has led to the development of new technologies to help answer this requirement. As a result, electronic gate feature sizes have shrunk while the resulting gate switching speeds and on chip packing densities have increased. The interconnection of these gates, however, has become a limiting factor as electronic interconnects approach their fundamental limits. This is due to the increased power consumption, impedance mismatching, crosstalk, and dispersion problems caused by increasing the packing densities and speed of electronic gates.

The use of optical interconnects may alleviate the interconnection bottleneck experienced with electronic interconnects.[1] Optical interconnects offer several attractive advantages. For example, since photons do not interfere with each other, optical interconnects may cross without signal interference. Optical interconnects do not exhibit the capacitive loading and mutual interference effects present in electronic interconnects. Also, optical interconnects out of plane allow for a high degree of fan-out between processing elements.

Interconnects, in general, are constructed in a hierarchical fashion. The type of interconnect used depends upon the interconnect level and the specific architecture being implemented. Optical interconnects have been proposed for use at the chip, board, and rack levels in many different types of architectures.[2,3,4,5] In all of these schemes, the optical interconnect generally consists of a source, detector, and a channel which provides the actual interconnection

between the source and detector. Sources and modulators such as laser diodes, vertical cavity surface emitting lasers (VCSELs), and quantum well modulators such as the symmetric self-electro-optic effect device (S-SEED)[6] exist in array formats. Likewise, high speed detectors exist in array formats as well as interconnects such as two dimensional microlens arrays or Dammann gratings.

The work presented here focuses on a gate to gate level interconnect as illustrated schematically in Fig. 1-1. The figure is a representation of a 3-D optical processor in which cascaded arrays of optical logic gates or smart pixel devices are interconnected optically in free space. At each processing plane, binary 1's and 0's are created by modulating the intensities of the free space optical signals. Optical interconnects then guide these signals to successive planes.

LOGIC PLANES

Accesion For		
NTIS CRA&I	☑	
DTIC TAB	☐	
Unannounced	☐	
Justification		
By		
Distribution /		
Availability Codes		
Dist	Avail and / or Special	
A-1		

INTERCONNECT OPTICS
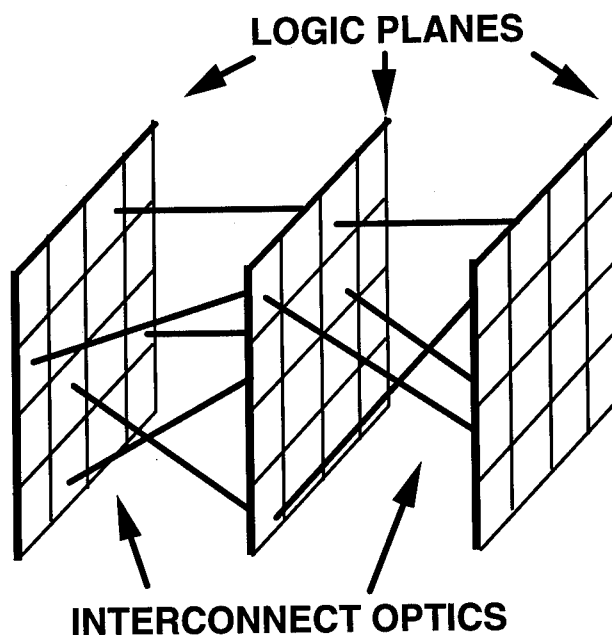
Fig. 1-1 3-D optical computing model

In this effort the various components needed to produce a free space optical processor of a related effort[7] which also follows the model of Fig 1-1 were explored. In section two of this report the characterization of S-SEEDs, which were used as the optical logic gates, is discussed. In sections three and four the theory and fabrication of diffractive microlens arrays are presented. Such diffractive elements are one possible candidate for forming the interconnect channels needed to steer optical signals from plane to plane. VCSEL based optical sources are discussed in section five. Conclusions follow in section six.

2.0 SEED EVALUATION

S-SEEDs consist of two SEEDs connected in series. Device inputs and outputs are both composed of a pair of beams, with each input beam focused on a SEED window. In this symmetric configuration, one SEED window is in a high reflectivity state, while the other is in a low reflectivity state. If the power of both of the input beams is equal, the state of the S-SEED is read-out and remains unchanged. If, however, the high reflectivity window is illuminated with more power than the low reflectivity window it is connected to, the state of the S-SEED toggles with the reflectivities of the windows interchanged.

Experiments concentrated on studying S-SEED device operation, and performing device evaluation from a systems perspective. A diagnostic microscope setup was designed and constructed for this purpose. This is schematically represented in Fig 2-1. Melles Griot 850 nm laser diodes were
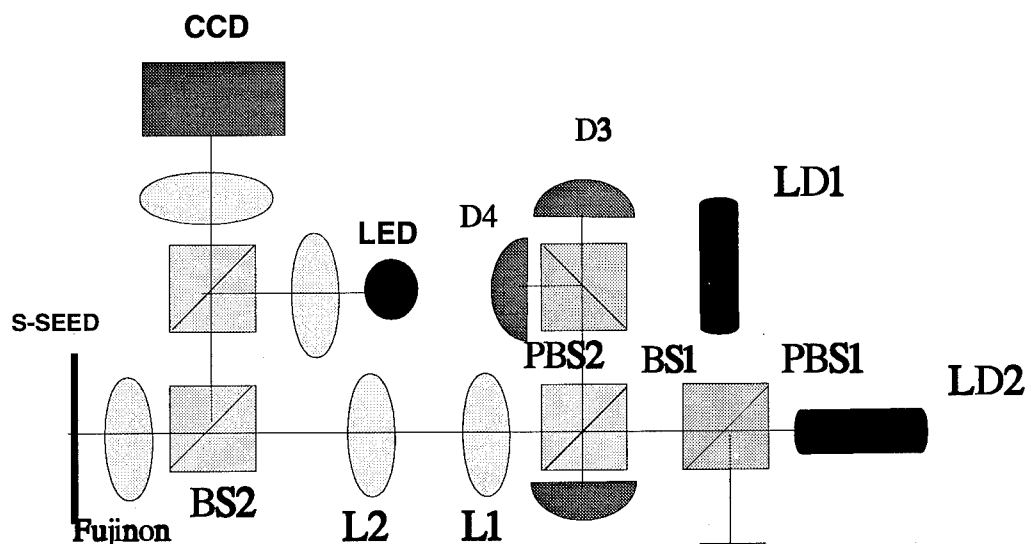
Fig. 2-1 S-SEED diagnostic microscope layout.

used for laser diodes LD1 and LD2. The diodes were packaged in sealed

assemblies which contained both TE coolers for wavelength stability and

anamorphic optics to provide collimated output. The laser diodes were oriented

so that their polarizations would be orthogonal to each other; LD1 was polarized

in the s-direction and LD2 was polarized in the p-direction. These two beams

where then combined at polarization beam splitter PBS1 as shown in the figure.

Halfwave plates were used in front of the lasers to rotate their polarizations and

thus control the amount of power coupled into the rest of the system by PBS1.

The power rejected by PBS1 was incident on detector D1 and was used to

calibrate incident power falling on the devices. The two collimated beams

passed into the system by PBS1 traveled through lenses L1 and L2, beam

splitter BS2, and entered a 7.79 mm focal length Fujinon objective lens. This

infinity corrected objective focused the collimated beams into diffraction limited

5

spots on the windows of a S-SEED device. Alignment of the beams from LD1 and LD2 onto the SEEDs was accomplished by angularly translating the position of LD1 using PBS1 so that it could be aligned on a S-SEED relative to LD2. Lenses L1 and L2 were used as relay lenses to handle off axis collection and help reduce vignetting over large tuning fields. The angular translations produced from PBS1 were then translated into spatial translations of the focused spots by the objective lens The beams were aligned such that the s-polarized light from LD1 was focused on the left window of the S-SEED and the p-polarized light from LD2 was focused on the right window of the device. Since the objective was infinity corrected, the outputs reflected off the S-SEED were collimated after passing back through the objective. Beam splitter BS2 then split the output into two paths. The upper path consisted of imaging optics, a CCD camera, and a LED. The imaging optics and CCD camera allowed the visual alignment of the beams from LD1 and LD2 onto the S-SEED windows and provided the ability to view the output from the device. The LED provided incoherent illumination for the microscope system thus allowing the devices to be viewed. The second path from BS2 returned the beams back to the front of the system to BS1. At BS1 the output was reflected to a polarization sensitive detector assembly consisting of PBS2 and two silicon detectors. PBS2 directed the s-polarized light from the left SEED window onto detector D3. Likewise, the p-polarized light from the right SEED window was directed onto detector D4. This allowed for a mechanism to perform measurements based on the reflectivities of each window in a S-SEED device.

Measurements involving wavelength were performed using a Wavemeter

scanning Fabre-Perot interferometer which received its signal via beamsplitter BS2. The wavelengths of the two laser diodes used were individually measured by this path blocking one laser diode at a time. Several measurements were made to verify reproducibility of laser wavelength for a given drive current level. The output wavelengths were found to be repeatable. A spectrum analyzer was later used in place of the wavemeter to examine mode hopping behavior of the drive lasers. Mode hoping occurred severely at a drive current of 25 mA for both lasers. This behavior was confirmed by the manufacture's data.

After the drive lasers were characterized, the next series of experiments dealt with basic S-SEED switching. Using an HP4145B semiconductor parameter analyzer, the devices were first forward biased to confirm that the devices were functional. Forward biasing a S-SEED causes its windows to luminance. The devices were then reversed biased and switching was demonstrated using the diagnostic microscope discussed above. S-SEED switching was accomplished by leaving the output of LD1 constant and then increasing the power of LD2 until it was greater than that of LD1, causing the S-SEED to switch. The device was then toggled back into the opposite state by lowering the power on LD2 to the point where switching occurred again. Device switching was observed visually via the CCD camera. Switching was also observed electronically using detectors D3 and D4.

A thermo-electric cooler unit was designed and built to keep the SEEDs at a constant temperature. SEED contrast ratio experiments were then performed. The wavelengths of both drive lasers were set to be as close as possible (limited

to three significant digits) for this experiment. The SEED reflectivity was measured first with the device in the high state. The device was then switched and measured in the low state. From this method, peak contrast was measured at approximately 851 nm. Experiments were performed over a wavelength range of 849-854 nm as shown in Fig. 2-2.

Wavelength vs. Contrast Ratio

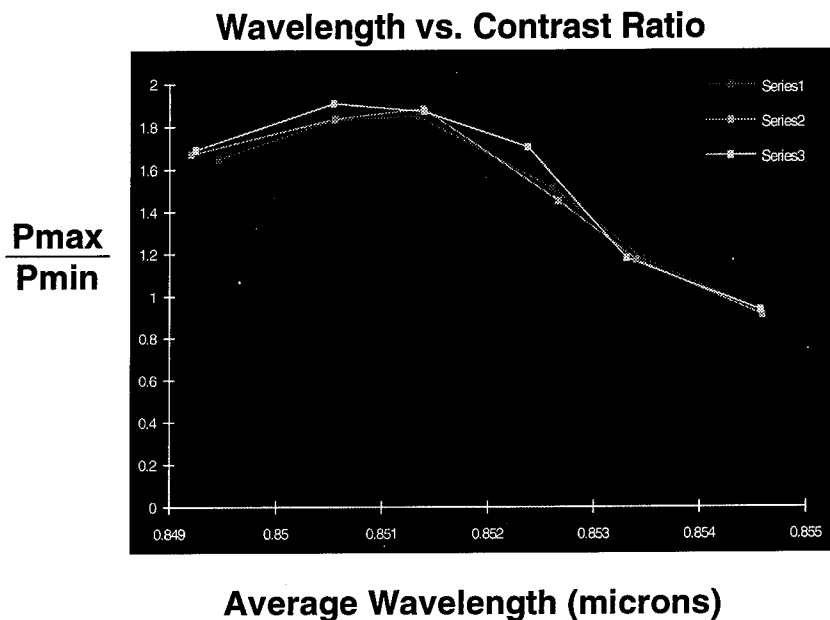$$\frac{Pmax}{Pmin}$$

Average Wavelength (microns)

Fig 2-2. SEED contrast versus wavelength measurements

The same tests were performed on three different SEEDs on the same array. As shown in Fig 2-3, the same behavior was observed for different SEEDs on the same array.
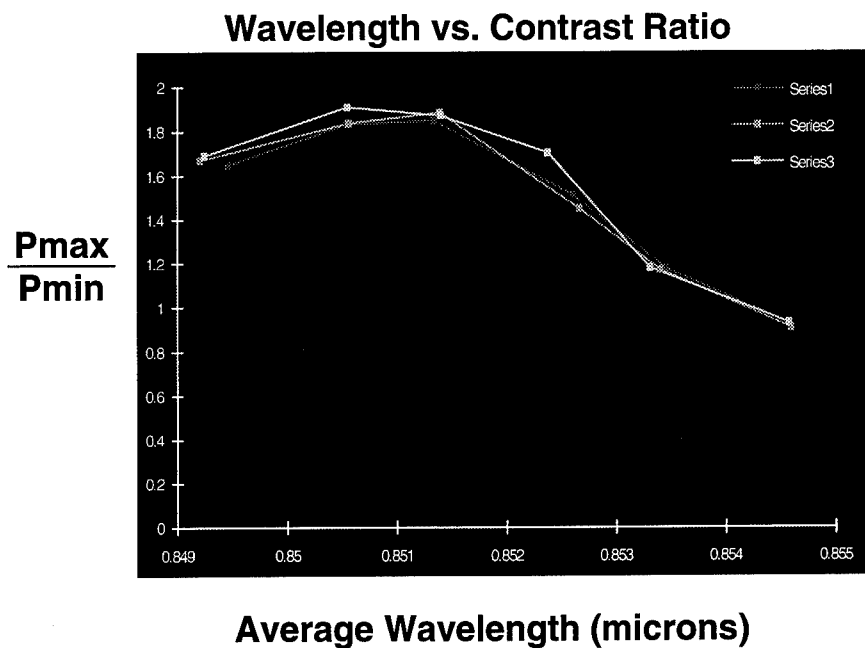
Wavelength vs. Contrast Ratio

$$\frac{\text{Pmax}}{\text{Pmin}}$$

Average Wavelength (microns)

Fig 2-3 SEED contrast versus wavelength for different array elements.

3.0 DIFFRACTIVE LENS THEORY

3.1 Binary Diffractive Lenses

A binary diffractive lens maybe thought of as a Fresnel Zone Plate (FZP) implemented as a phase structure.[8] Instead of modulating the transmission characteristics of an incident beam by blocking every other zone like in the FZP, the phase Fresnel lens consists of transparent zones where the thickness of alternating zones is modulated instead. This phase modulation between successive zones causes the amplitude of light from each zone arriving at point P to be positive and allows the coherent summation of all the amplitudes from each zone at point P. Hence a phase Fresnel lens will have double the

9

amplitude and four times the irradiance at point P than an absorptive FZP.

The radii for each zone in a FZP can be calculated by considering a FZP illuminated by a monochromatic plane wave (Figure 3-1). The focal length of the plate at wavelength λ is f and its radius is r_m, which is the radius of the mth or last zone of the plate. The optical path difference (OPD) between a ray going through the center of the plate and one from the edge is given by,
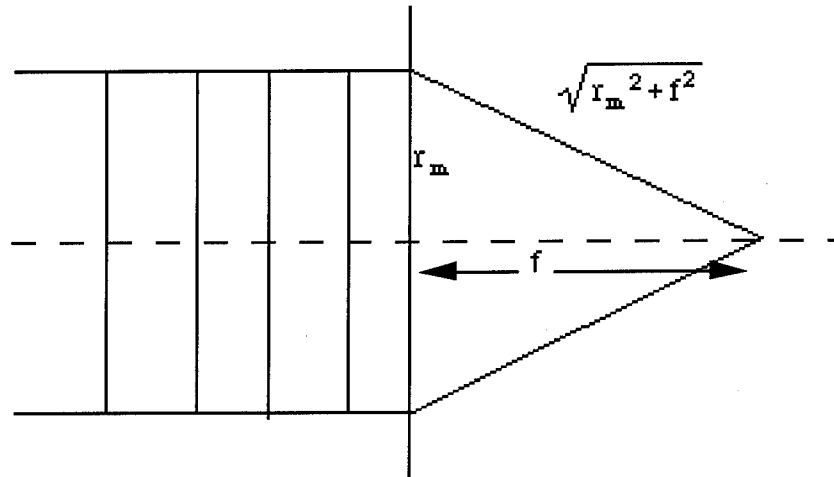

Figure 3-1 FZP focusing an incident plane monochromatic wave.

$$OPD = \sqrt{r_m^2 + f^2} - f.$$
\hfill 3.1

The incident plane wave is thus converted into a converging wave with a resulting phase retardation of

$$\phi = \frac{2\pi}{\lambda} [\sqrt{r_m^2 + f^2} - f]$$
\hfill 3.2

The zone theory of Fresnel states that the phase difference from the center of the lens to the mth zone must be equal to a multiple of π. Setting Equation 3.2 equal to _m, and solving for r_m, the radius of the mth zone, gives,

10

$$r_m = \sqrt{(\frac{m\lambda}{2})^2 + m\lambda f}$$.   3.3

The maximum number of zones for a given focal length and radius is calculated by solving Equation 3.2 for m, the number of zones,

$$m = \frac{2}{\lambda}(\sqrt{r_m^2 + f^2} - f)$$ 3.4

These equations describe the parameters needed to construct a phase Fresnel zone plate or binary diffractive lens. The term binary lens arises from the two level phase structure (zero and π) of the lens as illustrated in Figure 3-2. It consists of transparent circular zones with a square wave profile. The thickness change between alternating zones induces the necessary π phase shift between successive zones. Because of its symmetry, the binary lens directs equal amounts of incident light into the +1 and -1 orders. The resulting diffraction efficiency of a binary lens is 40.5%.
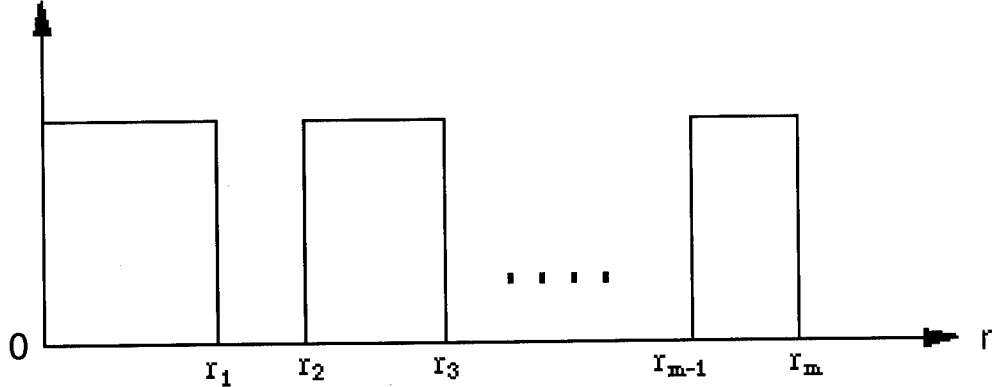

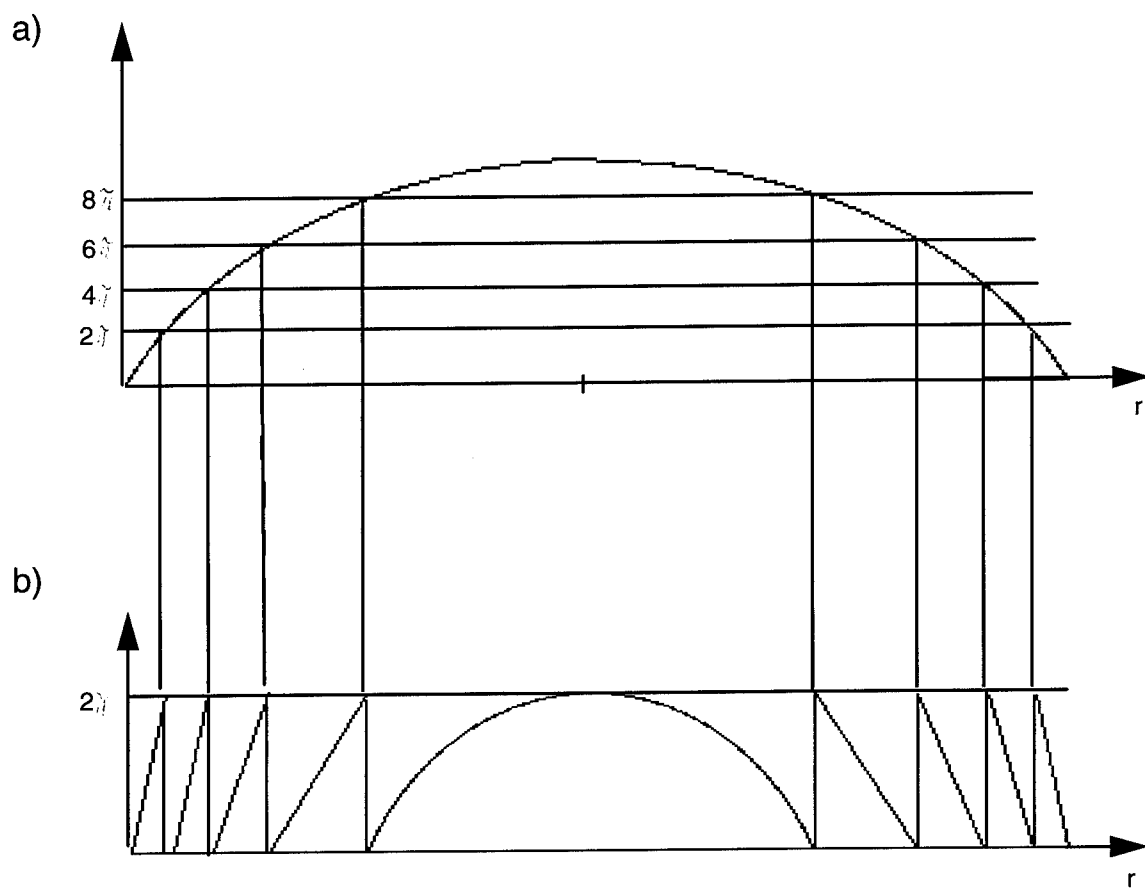Figure 3-2 Cross section of binary diffractive lens.

a)

8 π
6 π
4 π
2 π

r

b)

2 π

r

Figure 3-3 (a) Phase profile of refractive lens. (b) mod 2π phase profile of kinoform.

3.2 Multi-level Diffractive Lenses

A blazed diffraction grating is designed to direct all incident light into a desired diffraction order. A kinoform is a computer generated holographic version of a blazed grating which can be made to act as a lens.[9,10] A kinoform can be thought of as a phase FZP made as a blazed structure which results in a high efficiency diffractive lens.[11] Since the function of the kinoform is to perform as a lens, it is expected that the transmittance function and phase profile of the kinoform will be similar to that of a conventional refractive lens.[12] The phase profile of a refractive lens is quadratic and is given by,[13]

$$\varphi = \exp[-j\frac{k}{2f}(x^2+y^2)] \qquad \text{[3.5]}$$

The phase profile of a kinoform is defined as modulo 2π of the phase profile of the refractive lens; i.e. every time the phase profile of the refractive lens reaches a multiple of 2π, the phase of the kinoform returns abruptly to zero (Figure 3-3). The theoretical diffraction efficiency of a kinoform is 100% since it has an ideal blazed profile that directs all incident light into the first diffraction order. However, the continuous structure makes the kinoform difficult to produce.

To facilitate in the production of diffractive lenses, we may approximate the continuous kinoform profile with that of a quantized step profile.[14] Figure 3-4a is an example of a 2 level approximation to a continuous phase profile. Likewise, Figure 3-4b illustrates a
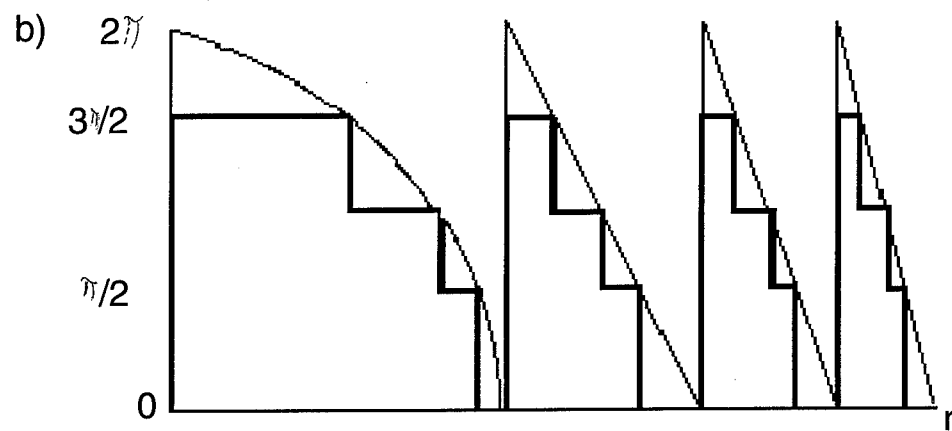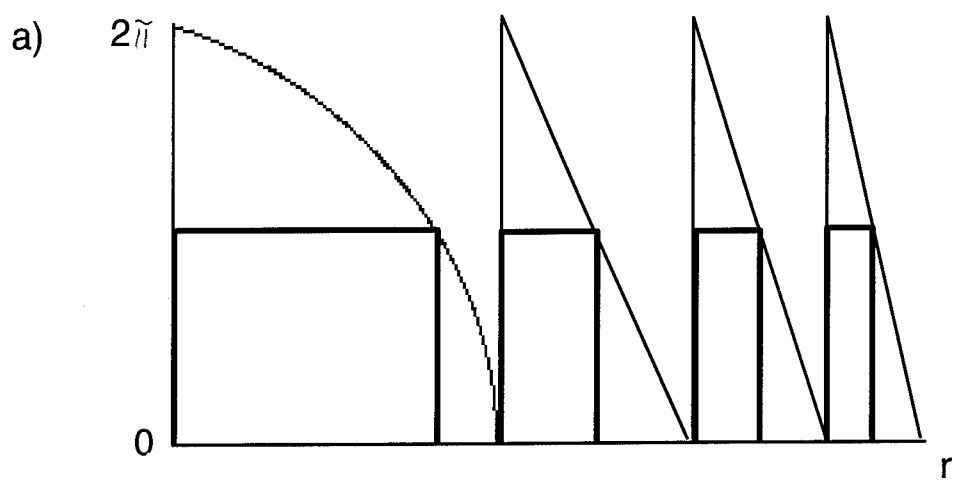
13

Figure 3-4 (a) Binary approximation to kinoform (b) 4 level approximation.

four level approximation. As the number of quantized steps, N, increases, the lens more closely approximates the continuous kinoform phase profile and the diffraction efficiency of the element will approach 100%.

As will be discussed in more detail later, a multilevel diffractive lens is fabricated using a set of binary masks. Each mask produces two phase levels. Thus, M masks are needed to produce $2^M = N$ phase levels. A two step (N=2) binary lens therefore only requires a single mask, a four level element (N=4) requires two masks and similarly for N=M.

The transition points for the boundaries of each zone in a multilevel element are calculated by examining the phase function given by Equation 3.2. For the case of the binary lens already discussed, the zone boundaries were determined by setting Equation 3.2 equal to multiples of π to satisfy the zone theory of Fresnel. It can be seen from Figure 3.4 that the size of these zone boundaries decreases as the number of levels increases. With each successive mask, the zone widths decrease by a factor of two, and two more phase levels are added. Since every mask produces 2 phase levels, the boundary of each zone occurs when the phase function in Equation 3.2 equals π/M. Equivalently this may be expressed as

$$\varphi = \left(\frac{2\pi}{\lambda}\sqrt{r_m^2+f^2} - f\right) = \frac{m\pi}{2^{M-1}}.$$
3.6

Solving Equation 3.6 for r_m and m as before gives the boundary for each zone and the maximum number of zones created by M masks,

$$r_m = \sqrt{\left(\frac{m\lambda}{2^M}\right)^2 + \frac{fm\lambda}{2^{M-1}}}$$ 3.7

$$m = \frac{2^M}{\lambda}\left(\sqrt{r^2_m + f^2} - f\right).$$ 3.8

For M=1, a binary lens, Equations 3.7 and 3.8 reduce to Equations 3.3 and 3.4. Thus, Equations 3.7 and 3.8 may be used as a general description for a N level diffractive lens.

3.3 Fabrication

The zone boundaries for the desired N level diffractive lens are calculated for M masks using Equation 3.7. This data is then converted into a format that can be read by an electron beam writing machine. The electron beam writer approximates the circular zones of the diffractive lens by using chains of multi-sided polygons[15] and creates a set of binary amplitude masks defining the structure of the lens. The resolution limit of the electron beam writer determines the smallest feature size possible for a diffractive lens. Fabrication technology limits the smallest multimask step size to approximately 0.5 μm.[16] The minimum mask feature size for a diffractive lens with numerical aperture NA occurs at the lens edge on the Mth mask and is

$$fmin = \frac{\lambda}{NA\ (2^M)}.$$ 3.9

Thus the lens must be designed so fmin > 0.5 μm.

Contact printing is the next step in the fabrication of the diffractive lenses. A mask is illuminated with a deep ultraviolet light source which exposes the mask pattern into a layer of photoresist on a glass substrate as shown in Figure 3-5.

16

Assuming positive type resist, the regions of exposed photoresist under the clear portions of the mask dissolve upon chemical development leaving the unexposed portions of photoresist. The remaining photoresist pattern serves as mask stop for the etching process which follows.

The etching process dissolves away the glass substrate wherever there is no photoresist and thus transfers the pattern directly into the glass substrate. To induce the proper phase shift on an incident field, the depth of the surface relief pattern must be carefully controlled. If the glass substrate is treated as a plane parallel plate, the phase delay experienced by a field traveling through the glass is

$$\phi = \frac{2\pi}{\lambda}(n-1)d \, ,$$
3.10

where n is the index of the substrate and d is its thickness. Setting this equal to $(2\pi/2^M)$, the phase height of a step for the Mth mask, and solving for the thickness d_M gives

$$d_M = \frac{\lambda}{2^M(n-1)} \, .$$
3.11

This is the etch depth required after exposing mask number M. After etching the substrate to this required depth, the remaining photoresist is removed. This process is then repeated M times for an N level element (since each mask produces 2 phase levels).
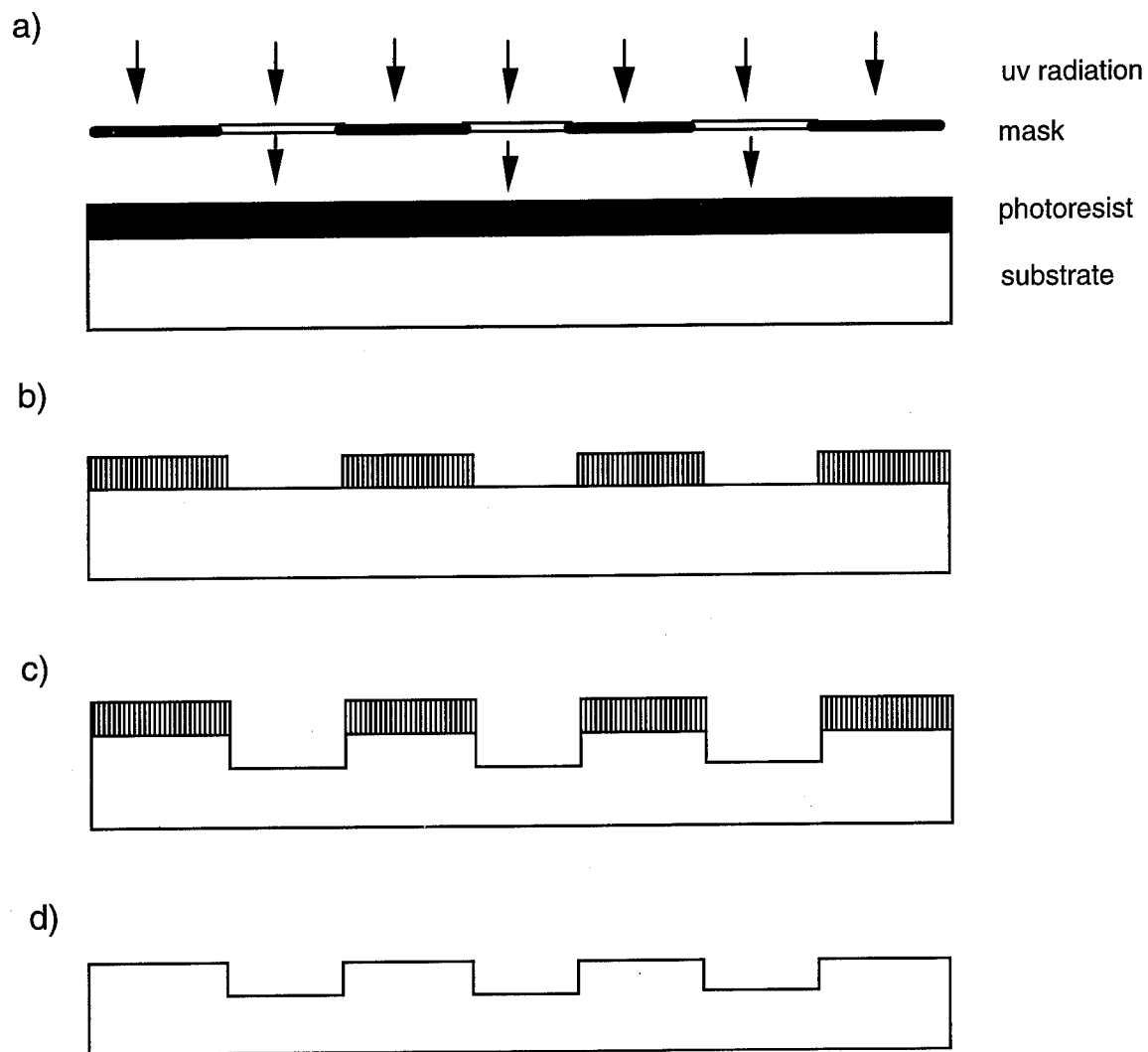
a)

uv radiation

mask

photoresist

substrate

b)

c)

d)

Figure 3-5 Fabrication process for binary lens. (a) mask exposure
(b) development (c) etch (d) photoresist removal.

4.0 EXPERIMENTAL FABRICATION AND TESTING

In this section, the experimental procedure developed for fabricating diffractive lenses via photolithography is presented. While photolithography is not the only method employed to fabricate diffractive lenses, it is a commonly used method and the one employed here.

4.1 Mask Generation

The first step in fabricating a diffractive lens by photolithography is to generate a mask set that physically describes the lens. Two, four level diffractive lens designs were produced. One set of lenses was designed to operate at a wavelength of 670 nm and the other to operate at a wavelength of 780 nm. Since the lenses were designed to contain four phase levels, each mask set consisted of two masks with alignment marks which were necessary to achieve proper registration between successive masks. Several different alignment marks were examined for use (Figure 4-1). A common element to each configuration is the use of symmetry (Since the human eye is very sensitive to detecting asymmetry in a high contrast pattern).[17] Detection of asymmetry in the overlying alignment marks indicates misalignment between successive substrate exposures.
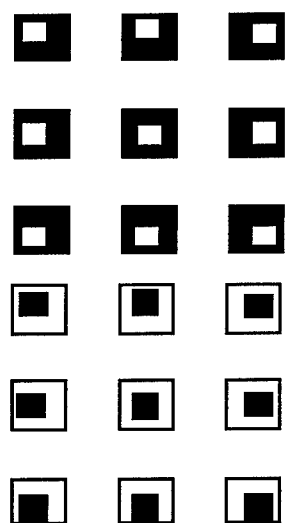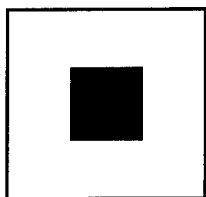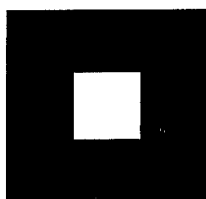
mosiac
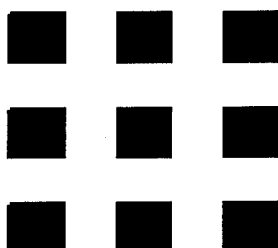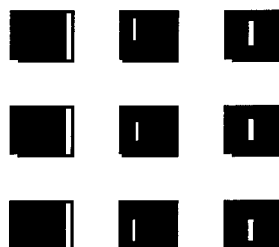
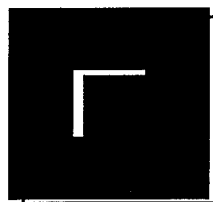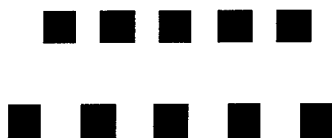aligned   misaligned

square within a square

aligned   misaligned

vernier

aligned   misaligned

Figure 4-1 Three different alignment marks. The left column contains the alignment mark pairs. The center column shows the marks when they are aligned with each other. The right column illustrates when the marks are misaligned with respect to each other.

Lens arrays of 1x6 and 4x4 were designed for both wavelengths. The zone radii for each was calculated using a program written in MATLAB. The program allows the user to input the desired lens wavelength, diameter, and NA and then outputs the appropriate zone radii. These zone radii, along with drawings of the mask layout, were sent to a commercial mask maker for fabrication. The lens arrays and corresponding alignment marks in these drawings were then produced on a chrome on quartz mask using electron beam lithography.

4.2 Substrate Preparation

Substrate preparation and all fabrication processes thereafter were performed in a class 100 clean room to prevent particle contamination. Using a process similar to that outlined by Roncone,[18] the glass substrates are first soaked in deionized (DI) water and 15 drops of *Micro* [19] cleaner for five minutes to help loosen surface contaminants. Each sample is then scrubbed lightly by hand, while wearing gloves, and rinsed thoroughly in DI water. Next the samples are placed in fresh DI water and *Micro* and sonic cleaned for four minutes for a more concentrated cleaning. After the sonic clean, the substrates are again rinsed in DI water. Another sonic cleaning in 100% ethanol (absolute) follows for four minutes. The ethanol is then drained and the substrates are baked in a vented oven at 180° C for one hour. The purpose of the ethanol rinse and following bake is to help remove water from the substrate. Any residual water will affect the adhesion of photoresist to the substrate.

4.3 Photoresist Deposition

Shipley Type P primer is first spun onto the substrate prior to photoresist deposition using a Solitec spinner. The primer is hexamethyldisilazane (HMDS) based and its purpose is to increase photoresist adhesion to the substrate by both removing any residual traces of water and by forming an interfacial bonding layer for the photoresist.[20] A syringe with a 0.2 µm filter is then used to apply two drops of primer to the center of the substrate. The primer is allowed to remain static on the substrate for 10 seconds and then is spun at 4000 rpm for 30 seconds. Four drops of Shipley 1811 positive type photoresist are then applied to the center of the substrate, again using a filtered syringe. The substrate is then immediately spun for 30 seconds at a selected speed. The speed selected determines the thickness of the photoresist film produced. Photoresist has a characteristic thickness versus speed curve based on its viscosity. The more viscous it is, the thicker it will spin at a given speed. Table 4-1 gives both experimentally obtained values and manufacturer supplied values of thickness versus speed data for the photoresist used. Experimental thickness measurements were made using a Tencor Alphastep 200 stylus profiler. Thickness vs. speed experiments were also conducted with thinner added to the photoresist. By adding thinner, the viscosity of the photoresist can by tailored to yield a desired photoresist thickness.

After the photoresist is deposited on the substrates, the substrates are

Photoresist Thickness (μm)

Speed (rpm)	Experimental Values	Manufacturer's Values
3000	1.2	1.23
4000	1.09	1.06
5000	0.94	0.93

Table 4-1 Speed vs. thickness values for Shipley 1811 photoresist.

baked again. This stage of the process is known as the soft-bake and it occurs for thirty minutes at 90° C.

4.4 Exposure and Development

A Karl Suss MJB3 mask aligner with a 325 nm UV light source was used to expose the mask onto the substrates. The mask aligner was used in a constant intensity mode at 15 mW/cm². The exposure time setting varied as a function of photoresist thickness. The thicker the photoresist layer, the longer the exposure time necessary to expose the mask pattern all the way through the photoresist to the glass substrate. To determine the necessary exposure time, a mask with linear gratings was exposed to a number of substrates, each for a different exposure time. The substrates were then examined using the stylus profiler to determine the proper exposure time. The proper exposure time was determined by examining the square well pattern formed in the photoresist by the mask exposure. If the height of the square well features in the photoresist was not equal to the known height of the photoresist, the exposure time used was insufficient. Using this procedure it was determined that the necessary exposure time for a photoresist thickness on the order of 1 μm was 15 seconds and 8

seconds for a thickness on the order of 0.6 µm.

After exposure, the samples were immersed in Shipley 352 developer for one minute. They were then immersed in DI water for another minute and then blow dried with nitrogen gas. A hard bake followed at 110° C for thirty minutes. Figure 4-2 presents a summary of the fabrication steps thus far.

A. Substrate Preparation:

1. Soak slides in DI water and 15 drops Micro for 5 minutes.
2. Scrub lightly while wearing gloves.
3. Sonic clean in fresh DI water and Micro for 4 minutes.
4. Rinse thoroughly with DI water.
5. Sonic clean in 100% ethanol for 4 minutes.
6. Drain and bake in a vented oven at 180° C for one hour.
7. Cool to ambient.

B. Photoresist Deposition:

1. Place 2 drops of primer on substrate. Let stand for 10 seconds. Spin dry at 4000 rpm for 30 seconds.
2. Place 4 of drops photoresist on substrate. Immediately spin for 30 seconds at appropriate speed for desired thickness.
3. Bake at 90° C for 30 minutes.
4. Cool to ambient. Place substrates in dark box.

C. Exposure and Development:

1. Deep UV exposure of substrate.
2. Immerse in developer at 21° C for 60 seconds.
3. Immerse in DI water for 60 seconds.
4. Blow Dry with N_2.
5. Hard bake at 110° C for 30 minutes.

Figure 4-2 Procedures for substrate preparation and development.

4.5 Binary Photoresist Gratings

Without the ability to etch, the realization of four level lenses was not possible. However, using the surface relief profile of the photoresist, the formation of binary lenses in photoresist was possible. The thickness of the photoresist necessary to produce a binary element with the proper phase modulation is calculated using Equation 3.11,

$$d_M = \frac{\lambda}{2^M(n-1)}$$ 4.1

In this case, M equals one since only one mask is necessary to produce a binary lens. The index of refraction of Shipley 1811 photoresist at 670 nm is approximately equal to 1.64.[21] Thus the necessary photoresist thickness is 0.52 µm for a wavelength of 670 nm and a thickness of 0.61 µm for a wavelength of 780 nm. The photoresist thickness was tailored to be close to these thickness values using the spinning parameters discussed in section 4.4.

A 4x4 array of lenses was produced in this fashion. Each lens in the array has a 500 µm diameter, 59 zones, and a f-number of 3.5.

4.6 Focal Length Measurements

The focal length of the microlenses was measured using the Foucault or knife edge test.[22] In the Foucault test, a knife edge placed behind an illuminated lens produces a characteristic shadow pattern or Foucault graph in image space. The shadow pattern allows the viewer to determine where the knife edge is with respect to focus (Figure 4-3). When the knife edge is inside focus, it will block the lower rays leaving the lens causing the shadow pattern to consist of a dark

region on top and bright pattern on the bottom. The opposite shadow pattern is obtained when the knife edge is placed outside of focus. When the knife edge is exactly at focus, the shadow pattern will be all dark.

Light from a 670 nm laser diode incident on a 500 μm pinhole was used to illuminate a single microlens at a time. A razor blade serving as the knife edge was placed on a x-y-z translation stage and positioned directly against the substrate. The knife edge was then translated away from the substrate until the focus point was located by observing the shadow patterns. The focal length was taken as the distance the knife edge was translated from the lens and was measured to be approximately 1.5 mm. This is in close agreement to the design focal length of 1.562 mm. The accuracy of this measurement was limited to the precision of the micrometer on the translation stage, which was 10 μm and the small thickness of the razor blade. Another limiting factor was determining the exact location of focus from the Foucault graph because of noise present from light scatter. This poor signal to noise ratio is a result of the relatively low diffraction efficiency of a binary element (i.e. 40.5%).

4.7 Diffraction Efficiency Measurement

To measure diffraction efficiency, light from a 670 nm laser diode was first coupled into 4 μm diameter single-mode fiber. A microlens array was placed one focal length from the output of the fiber, and a single lens in the array was illuminated at a time. Light intensity was measured at two locations behind the lens array with a silicon photodiode. The first measurement was taken with the

26

detector immediately behind the lens to measure the total power present in all diffraction orders. The second measurement was made two feet behind the lens to determine the power present in only the first diffraction order. The diffraction efficiency of each microlens was taken as the ratio of the power in the first diffraction order to the total power in all the orders. Table 4-2 gives the diffraction efficiencies from three experimental runs for several lenses on two different substrates. The average diffraction efficiency for the lenses on

	SAMPLE 1 $\eta_{MAX}=40.37\%$				SAMPLE 2 $\eta_{MAX}=40.39\%$			
LENS	#1	#2	#3	Average	#1	#2	#3	Average
1	36.88	36.82	36.798	36.83	38.69	39.01	39.21	38.97
2	38.48	37.31	37.36	37.72	39.46	38.92	39.52	39.3
3	38.18	38.21	37.65	38.01	39.51	38.89	39.3	39.23
4	38.98	38.96	38.64	38.86	39.72	39.49	39.65	39.62
5	38.63	38.6	38.83	38.69	39.75	39.55	39.65	39.65
6	37.33	39.13	38.94	38.47	39.78	39.21	39.55	39.51
7	38.32	37.48	38.13	37.98	39.62	39.39	39.9	39.64
8	37.78	37.62	38.06	37.82	39.27	39.65	39.59	39.50
9	38.01	37.87	38.27	38.05	39.52	39.08	39.37	39.32
10	37.87	38.14	37.82	37.94	39.27	39.39	39.11	39.26
11	37.52	38.59	38.44	38.18	38.95	39.05	38.77	38.92
	Total Average= 38.05% Standard Dev.= .54				Total Average= 39.36% Standard Dev.= .25			

Table 4-2 Diffraction efficiencies of diffractive lenses from two different samples. η_{Max} is the maximum theoretical diffraction efficiency
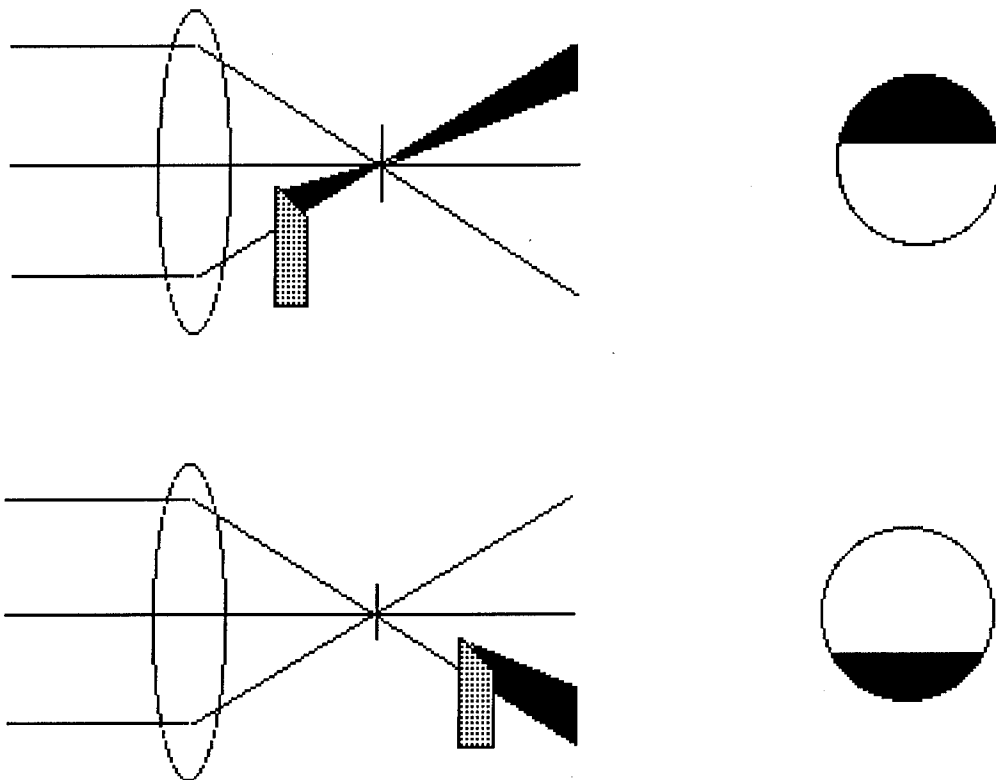
Figure 4-3 Knife edge test for perfect lens.

each substrate is very close to the calculated theoretical maximum diffraction

efficiency which takes into account errors in depth. The depth error for samples

one and two was less than 4%, and thus had very little effect on the maximum

possible diffraction efficiency. A third sample having a 13.9% photoresist depth

error was also tested. The resulting maximum theoretical diffraction efficiency
was lowered to 38.04%. Diffraction efficiency measurements of this sample are
given in Table 4-3 Again, experimental results were very close to theoretical.
The major source of error between experimental and theoretical values is
attributed to errors in measuring the actual photoresist depth and calculating
depth error. This is due to variations in photoresist thickness across
the substrate. Other sources of error arise from misalignment of the lenses
and losses due to Fresnel reflections.

SAMPLE 3 ηMAX=38.04%			
LENS #1	#2	#3	Average
1	36.49	35.66	37.5	36.55
2	36.73	36.96	36.36	36.82
3	35.57	35.97	36.36	35.97
4	35.14	35.51	35.23	35.29
5	36.9	35.66	34.78	35.78
6	36.2	35.66	34.78	35.55
7	35.8	35.21	35.16	35.39
Total Average= 35.89% Standard Dev.= .55			

Table 4-3 Diffraction Efficiencies for lenses with depth errors.

5.0 Vertical Cavity Surface Emitting Lasers (VCSELs) Used as SEED Drivers

VCSELs are solid state lasers that emit light perpendicular to the wafer they are made from. This is opposed to edge emitting lasers where the light is emitted in plane. Because VCSELs emit out of the plane, large two dimensional arrays of lasers can be made. These are particularly useful for optical interconnects or highly parallel optical computing schemes. Here we discuss considerations for using VCSELs to drive and readout SEEDs.

5.1 Laser Driver Circuit

In order to obtain uniform light output over time we chose to drive the VCSEL laser array with current sources. The contact resistance of each laser can vary across an array and from array to array. Using current sources to drive the lasers removes the variation in the contact resistance as a source of variation in light output since the output resistance of our current sources is at least 100,000 W and the laser contact resistance is usually less than 1,000 W. In addition the laser output becomes nonlinear with applied power when locally heated by the application of high current (power) as shown in figure 5-1. Since we were driving the lasers at a light level well below the maximum, the light output would be proportional to the current alone, assuming the overall temperature of the chip was held constant. So the current sources would allow the diode lasers to be operated without concern over the voltages required by individual lasers. This was an important requirement as the laser diode array

was not in hand until the latter half of the project and it was thought that as much as 10 volts might be required to drive some of the lasers.

5.2 Method

The temperature of the laser diode array was held constant with a TE cooler and an active controller. A thermistor mounted alongside the chip provided the controller with a measure of the chip temperature. The chip itself was mounted in a carrier with a metal base so that good thermal contact was maintained between the chip and the TE cooler.
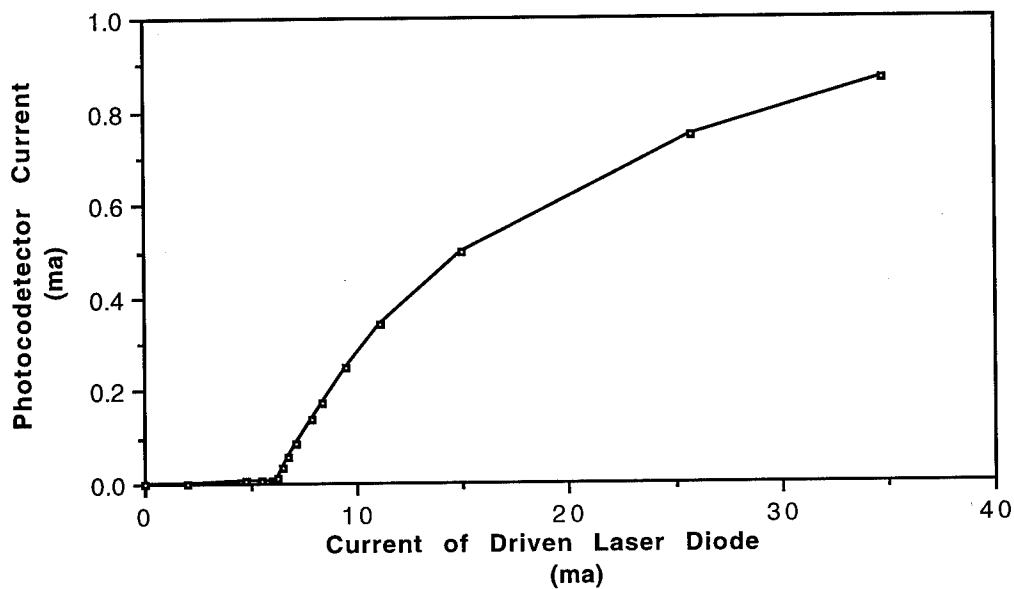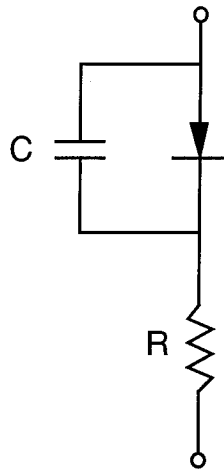
Figure 5-1

31

Figure 5-2. Simple Laser Model

Figure 5-2 shows a simple model for the laser diodes used. The capacitance (C) is no more than 1 pf and the resistance (R) is between 200 and 400 ohms for the devices we used. The forward diode drop was assumed to be about 1 volt. The lasers had a threshold current of about 10 ma and tended to enter a multimode condition usually before reaching 20 ma. This multimode condition caused an instability in the direction of polarization of the light output . We could not tolerate this as our system was sensitive to polarization. So we chose to drive the lasers with a current over a range of 12 to 16 milliamperes adjusting the current for uniformity of light output.
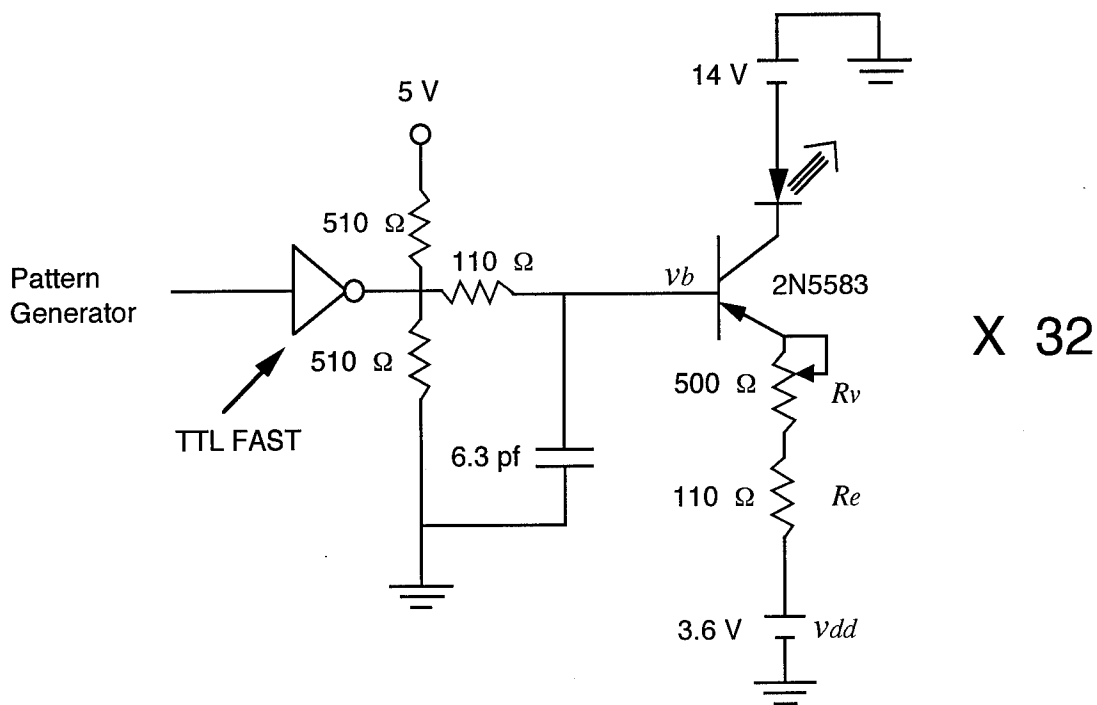
Figure 5-3. Laser Diver

Figure 5-3 shows the laser driver circuit as employed in the system. A collector current is "programmed" by asserting a voltage at the base of the transistor. This voltage, plus one diode drop, will appear at the emitter. The collector current is then

$$i_c \cong \frac{v_b + 0.6 - v_{dd}}{R_e + R_v}$$

where i_c is the collector current (and therefore the current through the laser diode), v_b is the base current, R_e is the emitter resistor, and R_v is a 500 W

33

potentiometer. The potentiometer adjusts the current from about 5 milliamperes to about 30 milliamperes. A logic pattern generator drives a FAST TTL inverting buffer that in turn drives the circuit from 0 to about 3 volts. The two 510 W resistors are added to keep the output of the TTL inverter at about 3 volts in its high state. The 110 W resistor and 6.3 pf capacitor on the base set the risetime of the circuit so that adjusting the potentiometer does not influence the risetime to any great degree. This circuit will easily drive the laser diodes to 50 MHZ square wave or to about a 100 megabits per second data rate. The pattern generator we used to drive the circuit is limited to a data rate of 50 megabits per second.
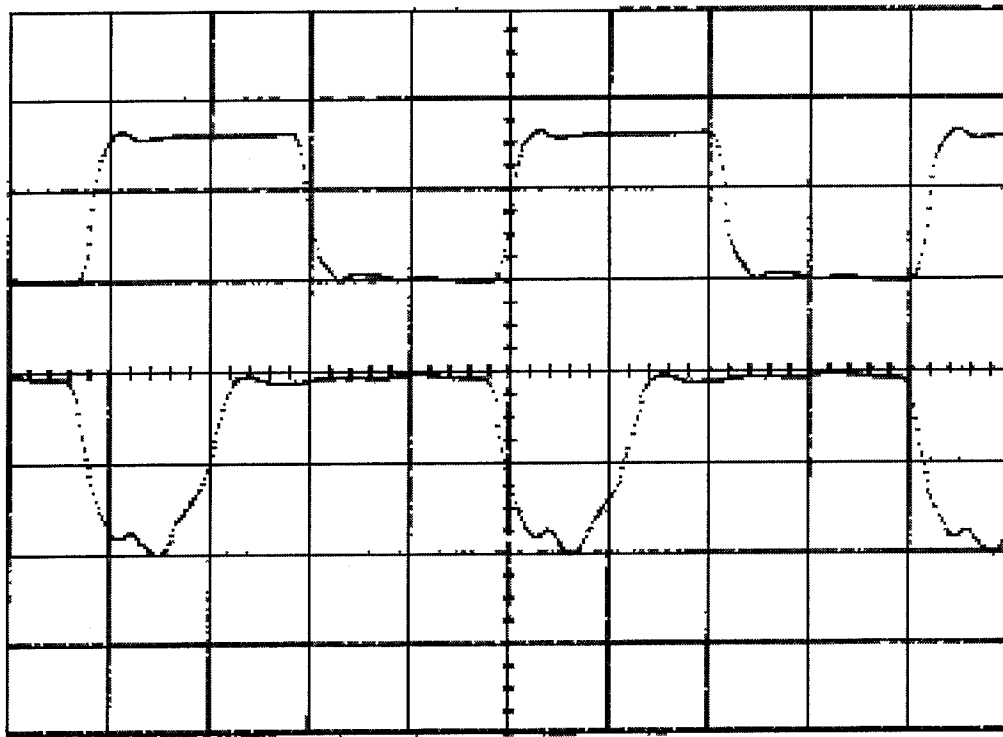

Figure 5-4. Upper trace is the VCSEL drive signal and the lower trace is VCSEL light out (down is more light). Horizontal is 5 ns/div, vertical is 5 v/div. Signal out is delayed by about 10 ns so negative going drive signal corresponds to light out. The shorter output signal occurs because the circuit band limits the drive signal to a sinusoid like signal and then clips it at the low voltage side of the signal producing a shorter output pulse than the input pulse.

The bottom trace in figure 5-4 shows the actual light output from a vertical cavity laser when driven by a 50 MHZ square wave. The laser was driven at high currents so that it was operating in the multimode condition mentioned earlier. Figures 5-5 and 5-6 show the linear polarization components of the same laser. These polarization components are aligned with the lattice axes. It can be seen that the vertically polarized modes start out strong but are quickly dominated by the horizontally polarized modes.
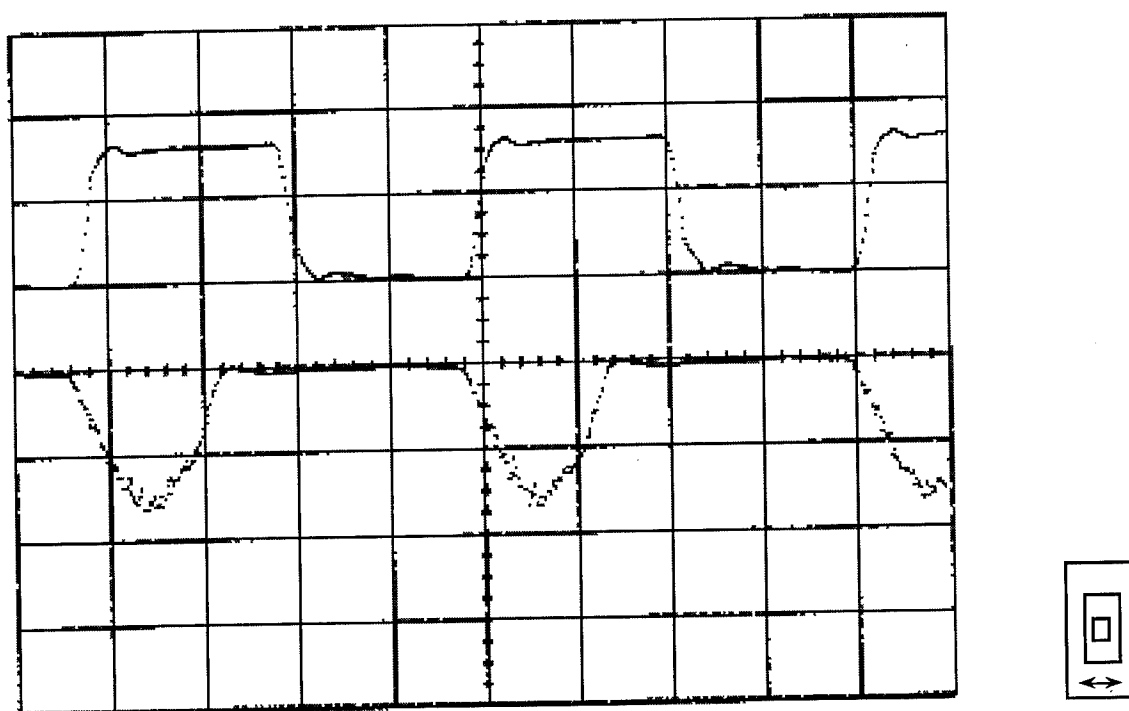

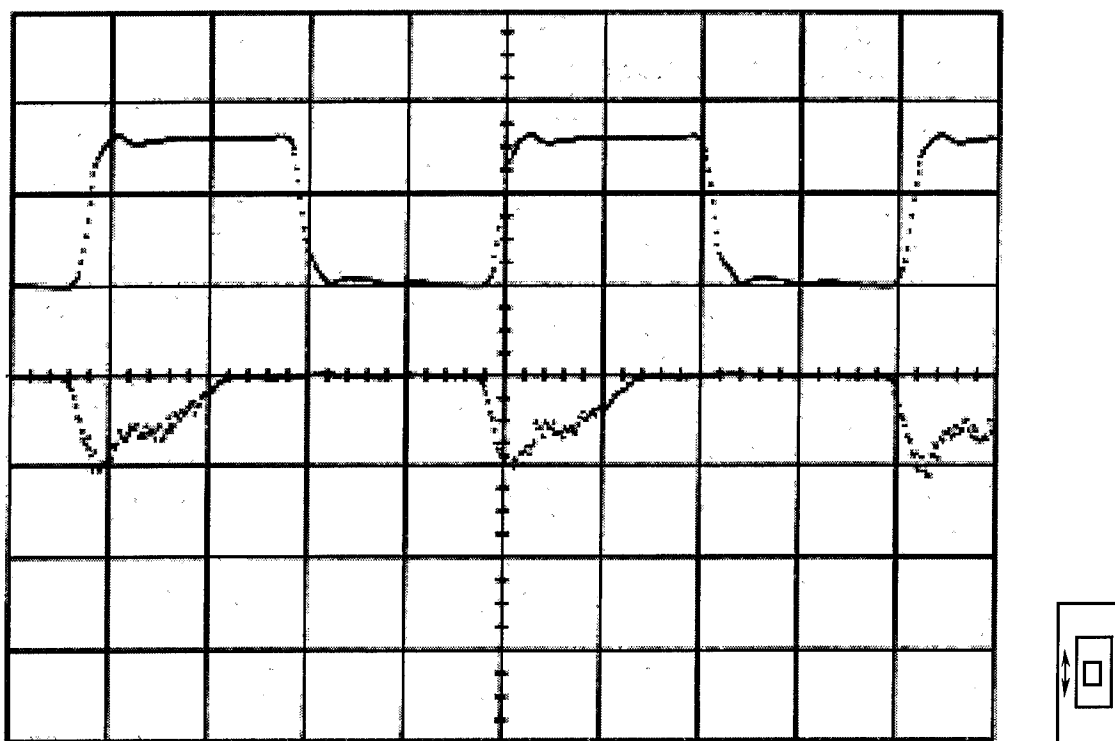Figure 5-5. Horizontally polarized output (bottom trace).

Figure 5-6. Vertically Polarized output (bottom trace).

5.3 Control of Wavelength

It is important that when using VCSEL arrays to read out SEEDs that the wavelength of the VCSELs be centered on the SEED band edge. The average wavelength for the array can be controlled by varying the array temperature but if the wavelength is different for each VCSEL across the array then not all the VCSEL wavelengths may be close enough to the wavelength of the SEED band edge. An example of wavelength variation across a VCSEL array can be seen in figure 5-7. The VCSELs near the brightest and the darkest corners are not usable as they are too far from the SEED wavelength center of approximately 8550 Å.
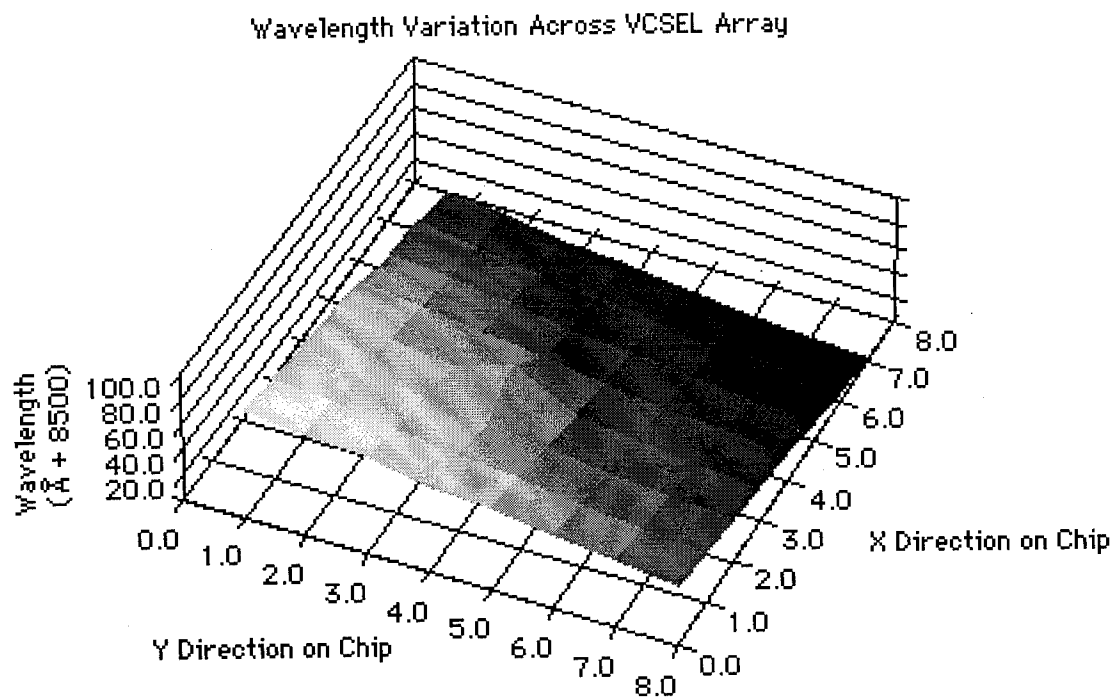
36

Figure 5-7.

6.0 Conclusion

Although optical computing has much potential for future high speed computing needs, it is still ultimately limited to the devices available. This report has focused on the study of a few key components used in the optical computing model of Fig 1-1. Experiments on S-SEEDs, VCSEL driving electronics, and diffractive optics have been presented. Each is a key component for the processor which is described in reference [7].

[1] J. W. Goodman , F. J. Leonberger, S. Y. Kung, and R. A. Athale, "Optical interconnects for VLSI Systems," Proc. IEEE **72**, 850 (1984).

[2] J. W. Parker, "Optical Interconnection for Advanced Processor Systems: A Review of the Espirt II Olives Program," Journ. Lightwave Tech. **9**, 1764 (1991).

[3] R. C. Kim, E. Chen, and F. Lin, " An Optical Holographic Backplane Interconnect System," Journ. Lightwave Tech. **9**, 1650 (1991).

[4] A. Dickinson and M. E. Prise, "Free-space Optical Interconnection Scheme," Appl. Opt. **29**, 2001 (1990).

[5] R. K. Kostuk, J. W. Goodman, and L. Hesselink, "Optical Imaging Applied to Microelectronic Chip-to-Chip Interconnects," Appl. Opt. **24**, 2851 (1985).

[6] A. L. Lentine, H. S. Hinton, D. A. B. Miller, J. E. Henry, J. E. Cunningham, L. M. F. Chirovsky, "Symmetric Self-Electro-Optic Effect Device: Optical Set-Reset Latch,"Appl. Phys. Lett. 52, 1419 (1988).

[7] J. M. Battiato, T. W. Stone, M. J. Murdocca, R. J. Bussjager, and P. R. Cook, "Free Space Optical System Based On Vertical Cavity Surface Emitting Lasers and Self-Electro-Optic Effect Devices," submitted to Applied Optics.

[8] K. Miyamoto, "The Phase Fresnel Lens," J. Opt. Soc. Am. **51**,17 (1961).

9 L. B. Lesem, P. M. Hirsch, and J. A. Jordan,Jr., "The Kinoform: A New Wavefront Reconstruction Device," IBM J. Res. Dev. **13**, 150 (1969).

10 H. Dammann, "Blazed Synthetic Phase-Only Holograms," Optik **31**, 95 (1970).

11 J. A. Jordan,Jr., P.M. Hirsch, L.B. Lesem, and D.L. Van Rooy , "Kinoform Lenses," Appl. Opt. **9**, 1883 (1970).

12 D. A. Buralli, G. M. Morris, and J. R. Rogers, "Optical Performance of Holographic Kinoforms," Appl. Opt. **28**, 976 (1989).

13 J. W. Goodman, *Introduction to Fourier Optics* (McGraw-Hill, New York, 1968,) p. 81.

14 L. d'Auria, J. P. Huignard, A. M. Roy, and E. Spitz, "Photolithographic Fabrication of Thin Film Lenses," Opt. Commun. **5**, 232 (1972).

15 S. M. Arnold, "Electron Beam Fabrication of Computer Generated Holograms," Opt. Eng. **24**, 803 (1985).

16 M. W. Farn, M. B. Stern, and W. Veldkamp, "The Making of Binary Optics," Opt. Photon. News, May 1991 p. 20.

17 M. Feldman, "Alignment Techniques in Optical and X-Ray Lithography" in *VLSI Electronics* vol. 16, Edited by N.G. Einspruch, (Academic Press, 1987,) pp.245-248.

18 Private communication with Ron Roncone, Optical Sciences Center.

19 *Micro* is a cleaner made by International Products Corp., Trenton, NJ.

20 Shipley product guide.

21 private communication with Rubin Castille , Shipley Corporation.

22 D. Malacara, ed.,*Optical Shop Testing*, 2nd ed.,(Wiley, New York, 1992) chap. 8.

Rome Laboratory

Customer Satisfaction Survey

RL-TR-_____

Please complete this survey, and mail to RL/IMPS,
26 Electronic Pky, Griffiss AFB NY 13441-4514. Your assessment and
feedback regarding this technical report will allow Rome Laboratory
to have a vehicle to continuously improve our methods of research,
publication, and customer satisfaction. Your assistance is greatly
appreciated.
Thank You

_____
_____

Organization Name:_____(Optional)

Organization POC: _____(Optional)

Address:_____

1.   On a scale of 1 to 5 how would you rate the technology
developed under this research?

     5-Extremely Useful   1-Not Useful/Wasteful

                    Rating_____

Please use the space below to comment on your rating. Please
suggest improvements. Use the back of this sheet if necessary.

2. Do any specific areas of the report stand out as exceptional?

                    Yes___ No_____

     If yes, please identify the area(s), and comment on what
aspects make them "stand out."

3. Do any specific areas of the report stand out as inferior?

                        Yes___ No___

     If yes, please identify the area(s), and comment on what aspects make them "stand out."

4. Please utilize the space below to comment on any other aspects of the report. Comments on both technical content and reporting format are desired.

MISSION

OF

ROME LABORATORY

Mission. The mission of Rome Laboratory is to advance the science and technologies of command, control, communications and intelligence and to transition them into systems to meet customer needs. To achieve this, Rome Lab:

a. Conducts vigorous research, development and test programs in all applicable technologies;

b. Transitions technology to current and future systems to improve operational capability, readiness, and supportability;

c. Provides a full range of technical support to Air Force Materiel Command product centers and other Air Force organizations;

d. Promotes transfer of technology to the private sector;

e. Maintains leading edge technological expertise in the areas of surveillance, communications, command and control, intelligence, reliability science, electro-magnetic technology, photonics, signal processing, and computational science.

The thrust areas of technical competence include: Surveillance, Communications, Command and Control, Intelligence, Signal Processing, Computer Science and Technology, Electromagnetic Technology, Photonics and Reliability Sciences.